Analysis of the Behavior of Undamped and Unstable High-Frequency Resonance in DFIG System

Song, Yipeng; Blaabjerg, Frede

Published in:
I E E E Transactions on Power Electronics

DOI (link to publication from Publisher):
10.1109/TPEL.2017.2654919

Publication date:
2017

Document Version
Accepted author manuscript, peer reviewed version

Analysis on the Behavior of Undamped and Unstable High Frequency Resonance in DFIG System

Yipeng Song, *Member, IEEE*, and Frede Blaabjerg, *Fellow, IEEE*

***Abstract* — As the wind power generation develops, the Doubly Fed Induction Generator (DFIG) based wind power system may suffer Sub Synchronous Resonance (SSR) and High Frequency Resonance (HFR) in the series and parallel compensated weak network. The principle and frequency of HFR have been discussed using the Bode diagram as an analysis tool. However, the HFR can be categorized into two different types: undamped HFR (which exists in steady state) and unstable HFR (which eventually results in complete instability and divergence), both of them are not investigated before. Since both the undamped HFR and unstable HFR are critical to the output wind power quality as well as the safe and reliable operation of the DFIG system, it is meaningful to discuss them using the Nyquist Criterion from two perspectives, 1) determining either the undamped HFR or the unstable HFR happens; 2) estimating the amplitude of the undamped HFR. The influence factors, including the weak network shunt capacitance, the current PI controller parameters are discussed when estimating the amplitude of the undamped HFR. The experimental and simulation results of a 7.5 kW down-scaled DFIG setup are provided to validate the analysis on the undamped HFR and unstable HFR.**

***Index Terms* — DFIG system impedance modeling; high frequency resonance (HFR); Nyquist Criterion; undamped HFR; unstable HFR.**

I. Introduction

Doubly Fed Induction Generator (DFIG) based wind power systems are increasingly installed globally [1]-[3] to achieve a higher portion of renewable energy in the power grid. For the purpose of ensuring a safe and reliable operation of the DFIG system, several improved control strategies have been demonstrated under the condition of grid voltage three-phase long-term steady state unbalance [4]-[6] and low voltage fault [7] as well as for the frequency support by virtual inertial control [8]. When connected to a weak network where the impedance is relatively large and requires serious attention, the Sub- Synchronous Resonance (SSR) [9]-[25] and the High Frequency Resonance (HFR) [26]-[28], might appear due to the impedance interaction between the DFIG system and the weak network.

The SSR which is typically below the fundamental frequency might appear when the DFIG system is connected to the series compensated weak network [9]-[25]. The method of harmonic linearization is adopted in [9]-[11] to develop the positive and negative sequences of the DFIG system impedance, and it is demonstrated that the rotor current control and the phase locked loop control with larger control bandwidth is more likely to produce the SSR, while less possibility of the SSR seems to appear at higher rotor speeds. The impedance modeling of the entire DFIG system and the series compensated weak grid network are reported in [12], and it is demonstrated that the interaction between the electric network and the converter controller contributes mainly to the SSR. Instead of using the Bode diagram, Ref. [14] adopted the impedance-based Nyquist stability criterion in order to explain the SSR phenomenon, i.e., to examine whether the ratio of the grid impedance to the DFIG system impedance encircles (-1,0) or not. Besides, an eigenvalue-based analysis was conducted in [15] to investigate the impact of SSR from the perspective of the grid and the DFIG. Three different modal resonances were also analyzed in [16], i.e., induction generator effect, torsional interactions and the control interactions. The SSR was analyzed from the quantitative perspective using an aggregated RLC circuit model of the series compensated weak network in [17], however no Nyquist Curve based stability criterion method is adopted.

On the other hand, the HFR may occur when the DFIG system is connected to the parallel compensated weak network [26]-[28]. As it is discussed in [26], the HFR is a consequence of the impedance interaction between the DFIG system and the parallel compensated weak network. The frequency of HFR is estimated based on the Bode diagram of the DFIG system impedance and the parallel compensated weak network impedance in [26]. It is found that the rotor speed is not sensitive to the HFR frequency since the DFIG system impedance shape at the high frequency range remains almost the same regardless of the different rotor speed, and the PI current controller parameters are also not important to the occurrence of the HFR. Note that only the occurrence and the frequency of the undamped HFR can be theoretically analyzed and estimated using the Bode diagram method in previous works [26]-[28]. The differences between this paper and [26]-[28] include two aspects, 1) only the undamped HFR, which is one of the two different types of HFR (undamped and unstable HFR), is discussed in [26]-[28]. The main contribution of [26]-[28] is to analyze the undamped HFR which exists in the steady state performance, and to propose the active damping strategy for mitigating the undamped HFR; 2) on the other hand, both the undamped HFR and unstable HFR are investigated in this paper, and this paper focuses on explaining whether the undamped HFR or the unstable HFR will happen under certain circumstances, and what are the influencing factors. Furthermore, the amplitude of the undamped HFR is also theoretically estimated in this paper.

The behavior of the HFR may often vary in practice, to be more specific, there are two possibilities in respect to the HFR, 1) one possibility is that the undamped HFR exists in

steady state, and the DFIG system is still able to operate with the inclusion of the HFR, unfortunately the output wind power can be distorted with a large amount of high frequency distortion in the output current and thereby jeopardizes the power quality. Besides that, the mechanical components of the DFIG system (shaft, bearing and gear-box) may experience high frequency vibrations, and even results in further mechanic damage; 2) the other possibility is that the unstable HFR may eventually result in instability, as a consequence the over voltage/current protection unit may cause a shut-down of the DFIG system and reduce the wind power output. Based on above explanations, it can be seen that the behavior of the undamped HFR and unstable HFR is critical to the output wind power quality as well as the safe and reliable operation of the DFIG system, and this topic is worthy discussing.

The Nyquist Criterion method has been adopted to analyze the occurrence of SSR in [14], and this method is implemented based on the small signal equivalent circuit of a DFIG system and a series compensated weak network, which is deduced based on the discussion of the impedance-based stability criterion for the grid-connected inverters in [29]. As it will be illustrated in this paper, the Nyquist Criterion method, compared with the conventional Bode diagram, can provide additional information about the amplitude of the undamped HFR and the occurrence of unstable HFR.

Therefore, the HFR will be investigated using the Nyquist Criterion method from two perspectives in this paper, 1) determining whether the undamped HFR (which exists in steady state) happens and results in the deterioration of the output wind power quality; or unstable HFR (which results in instability) happens and triggers the over-voltage/current protection which shuts down the DFIG system; 2) estimating the amplitude of the undamped HFR in steady state, then the wind power quality can be evaluated.

This paper is organized as follows: the general description and the impedance modeling of the DFIG system and the parallel compensated weak network are provided in Section II as a platform for the following discussion. Then, the HFR caused by the impedance interaction between the weak network and the DFIG system is illustrated based on the conventional Bode diagram method in Section III. Thereafter, the Nyquist Criterion based method is applied in Section IV to analyze the behavior of the HFR from the two perspectives mentioned above. The influence factors, including the weak network shunt capacitance and the current PI controller parameters, are also discussed in respect to the undamped HFR and the unstable HFR. The experimental and simulation setup of 7.5 kW down-scaled DFIG system are built up in order to validate the analysis on the undamped HFR and unstable HFR in Section V. Finally, the conclusions are given in Section VI.

II. General Description and Impedance Modeling of DFIG System

The general description of the DFIG system is necessary for the following discussion, and the impedance modeling of both the DFIG system and the parallel compensated weak network established in [26]-[28] need to be mentioned here as an analysis platform.

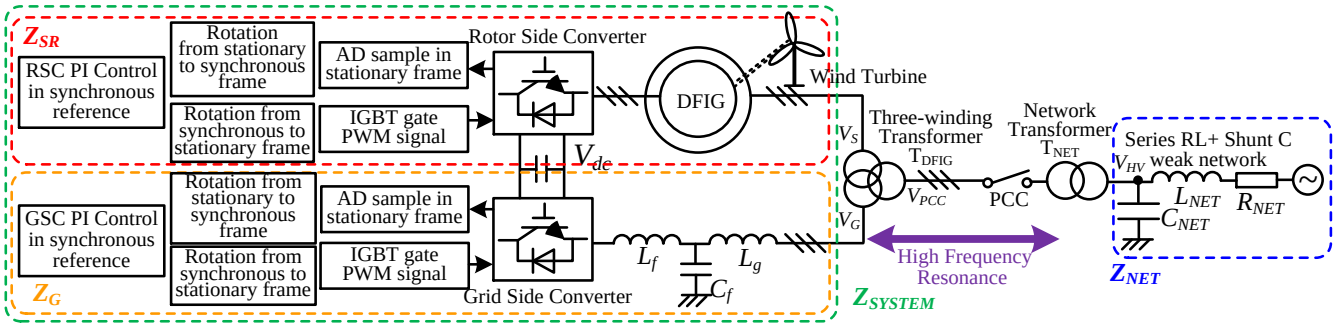

Fig. 1. Diagram of the DFIG system connected to a parallel compensated weak network.

A. General description of the DFIG system

The diagram of the investigated DFIG system and the parallel compensated weak network is shown in Fig. 1. The RSC controls the rotor voltage to deliver the DFIG stator output active and reactive power, the GSC provides the dc-link voltage. The three-terminal step-up transformer T_{DFIG} is connected between the DFIG stator winding, the LCL output terminal and the Point of Common Coupling (PCC) for the purpose of adjusting the voltage level of the DFIG system, the detailed parameters of this transformer can be found in Table I.

The parallel compensated weak network contains the network inductance L_{NET} and the network resistance R_{NET} in series connection, and the network shunt capacitance C_{NET} is connected between the transmission cables and the ground. A two-terminal transformer T_{NET} is connected between the PCC and the high voltage transmission cable, and the parameters of this transformer can also be found in Table I.

TABLE I. Parameters of 7.5 kW DFIG System

DFIG Machine			
Rated Power	7.5 kW	T_d	150 μs
R_s	0.44 Ω	R_r	0.64 Ω
$L_{\sigma s}$	3.44 mH	$L_{\sigma r}$	5.16 mH
L_m	79.3 mH	Pole Pairs	3
f_s	10 kHz	f_{sw}	5 kHz
LCL Filter			
L_g	7 mH	L_f	11 mH
C_f	6.6 uF		
Voltage level and ratios in T_{DFIG}			

V_G	400 V	V_S	400 V
V_{PCC}	400 V		
K_1	1	K_2	1
Current Controller Parameters			
K_{prsc}	2	K_{irsc}	5
K_{pgsc}	2	K_{igsc}	5
Parallel compensated weak network			
R_{NETP}	3 mΩ	L_{NETP}	1.5 mH
C_{NETP}	15,10,5,3μF		
V_{PCC}	400 V	V_{HV}	400 V
K_3	1		

B. *Impedance modeling of the DFIG system*

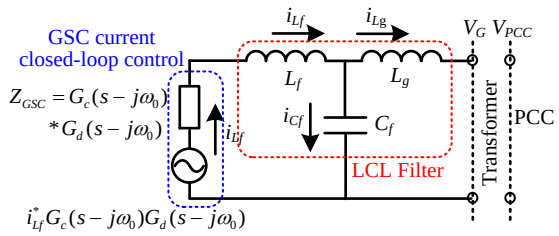

Fig. 2. Impedance modeling of the Grid Side Converter (GSC) equipped with LCL filter.

The grid part of the DFIG system contains the GSC and the LCL filter, its impedance modeling [26]-[28] in the stationary frame is presented in Fig. 2. Then, the impedance of the DFIG grid side in the stationary frame can be obtained as,

$$Z_G = K_1^2 \frac{Z_{Cf}\left(Z_{Lf}+Z_{GSC}\right)+Z_{Lg}\left(Z_{Lf}+Z_{GSC}\right)+Z_{Cf}Z_{Lg}}{Z_{Cf}+\left(Z_{Lf}+Z_{GSC}\right)} \quad (1)$$

where, $Z_{Cf} = 1/sC_f$, $Z_{Lf} = sL_f$, $Z_{Lg} = sL_g$. C_f is the LCL-filter capacitance, L_f is the converter side inductance, and L_g is the LCL grid side inductance. K_1 is the voltage ratio between V_G and V_{PCC} defined as $K_1 = V_{PCC}/V_G$. $Z_{GSC} = G_c(s\text{-}j\omega_0)G_d(s\text{-}j\omega_0)$, $G_c(s\text{-}j\omega_0)$ is the PI current controller containing the proportional part K_{pgsc} and the integral part $K_{igsc}/(s\text{-}j\omega_0)$, the parameters of K_{pgsc} and K_{igsc} can also be found in Table I. $G_d(s\text{-}j\omega_0)$ is the digital control delay of 1.5 sample period due to the delay of sampling and PWM update [26]-[28]. It needs to be pointed out that ω_0 is the grid fundamental component angular speed of 100π rad/s. The introduction of ω_0 is due to the reference frame rotation from the stationary frame to the synchronous frame, where the PI closed-loop current control is implemented. The control loop of the dc-link voltage and the grid synchronization in the GSC are neglected due to the slower dynamic response [26]-[28].

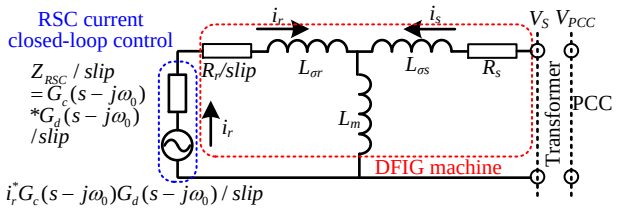

Fig. 3. Impedance modeling of the DFIG machine and Rotor Side Converter (RSC).

On the other hand, the impedance of the RSC and DFIG machine [26]-[28] in the stationary frame can be obtained in Fig. 3 as,

$$Z_{SR} = K_2^2 \frac{Z_{Lm}H+\left(R_s+Z_{L\sigma s}\right)H+Z_{Lm}\left(R_s+Z_{L\sigma s}\right)}{Z_{Lm}+H} \quad (2)$$

where $H = Z_{L\sigma r} + (R_r + Z_{RSC})/slip$; $Z_{RSC} = G_c(s\text{-}j\omega_0)G_d(s\text{-}j\omega_0)$, $Z_{Lm} = sL_m$; $Z_{L\sigma r} = sL_{\sigma r}$; $Z_{L\sigma s} = sL_{\sigma s}$. R_r is the rotor resistance, L_m is the mutual inductance, $L_{\sigma r}$ is the rotor leakage inductance, and $L_{\sigma s}$ is the stator leakage inductance. K_2 is the voltage ratio between V_S and V_{PCC} as defined $K_2 = V_{PCC}/V_S$. Since the rotor current control is implemented in the synchronous reference frame, it needs to be transformed into the rotor stationary frame using the slip angular speed expressed as [26]-[28],

$$slip = \left(s - j\omega_r\right)/s \quad (3)$$

where, ω_r is the rotor angular speed.

Therefore, since the RSC and DFIG machine Z_{SR} and the GSC and LCL-filter Z_G are connected in parallel, then the DFIG system impedance Z_{SYS} can be obtained based on (1) and (2) as,

$$Z_{SYS} = \frac{Z_G Z_{SR}}{Z_G + Z_{SR}} \quad (4)$$

C. *Impedance modeling of the parallel compensated weak network*

According to Fig. 1, the impedance modeling of the parallel compensated weak network [26]-[28] can be deduced as,

$$Z_{NET} = \frac{1}{K_3^2}\frac{\left(sL_{NET}+R_{NET}\right)/sC_{NET}}{sL_{NET}+R_{NET}+1/sC_{NET}} \quad (5)$$

where, $K_3 = V_{HV}/V_{PCC}$ is the voltage ratio between the high voltage V_{HV} in the long distance transmission cable and the PCC voltage V_{PCC}. R_{NET}, L_{NET} and C_{NET} are the network resistance, inductance and capacitance.

III. Conventional Analysis on the Frequency of HFR Using Bode Diagram

In the previous works in [26]-[28], the Bode diagram method is adopted to discuss the frequency of the HFR. The method is first to plot the Bode diagram curves of the DFIG system impedance and the parallel compensated weak network impedance, then to examine if the phase difference at the magnitude intersection point between the DFIG system and the weak network is equal or larger than 180° [26]-[28]. In order to better explain the HFR, the conventional analysis on the undamped HFR frequency using the Bode diagram method [26]-[28] is still mentioned here. The Bode diagram method and the proposed Nyquist Criterion method will also be compared and summarized in the following discussion.

The conventional analysis on the undamped HFR frequency is conducted based on the 7.5 kW DFIG system as shown in Fig. 4. As it can be seen, the impedance curves of the DFIG system and the parallel compensated weak networks have the magnitude intersection point at 1316 Hz when C_{NET} = 15 μF, 1575 Hz when C_{NET} = 10 μF, 2195 Hz

when C_{NET} = 5 μF, 2820 Hz when C_{NET} = 3 μF. The phase differences at these frequencies are all 180° and it will result in the occurrence of the HFR. This analysis method has been proved to be accurate and effective in [26]-[28], however only the frequency of the HFR can be identified using the Bode diagram method, while the resonance amplitude cannot be directly observed based on the Bode diagram in Fig. 4.

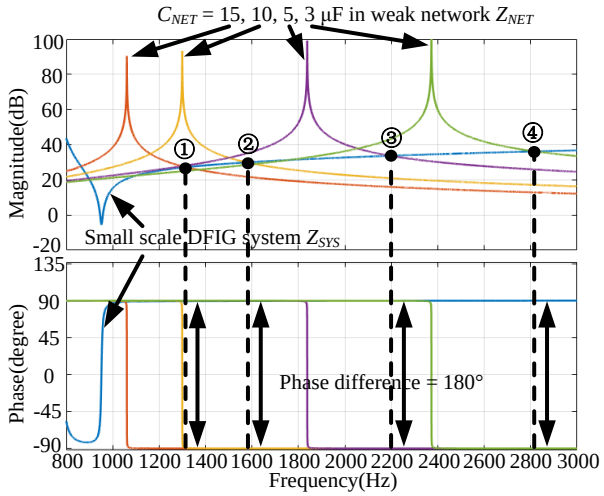

HFR in 7.5 kW small scale DFIG system
① When C_{NET} = 15 μF, HFR frequency = 1316 Hz;
② When C_{NET} = 10 μF, HFR frequency = 1575 Hz;
③ When C_{NET} = 5 μF, HFR frequency = 2195 Hz;
④ When C_{NET} = 3 μF, HFR frequency = 2820 Hz;

Fig. 4. Conventional analysis on the frequency of HFR between the 7.5 kW DFIG system and the parallel compensated weak network using the conventional Bode diagram method.

IV. Proposed Analysis of HFR Using Nyquist Criterion Method

In order to better investigate the undamped HFR and the unstable HFR, the Nyquist Criterion method is adopted in this paper. The Nyquist Criterion was proposed to analyze the stability of the grid-connected converters under weak network in [14] and [29]. Since both the grid-connected converter and the DFIG system can be modelled as one current source and the corresponding parallel impedance [29], the Nyquist Criterion method can be used here to analyze the undamped HFR and the unstable HFR in the DFIG system.

A. Small signal equivalent circuit of the DFIG system and the weak network

In order to apply the Nyquist Criterion method, the small signal equivalent circuit of the DFIG system and the weak network needs to be established first.

It is important to demonstrate that in the impedance modeling of the DFIG system grid part in Fig. 2 and the rotor part in Fig. 3, both of them contain a voltage source, which represents the rotor current closed-loop control output voltage $i_r^* G_c(s-j\omega_0)G_d(s-j\omega_0)/slip$ and the grid-side converter closed-loop control output voltage $i_{Lf}^* G_c(s-j\omega_0)G_d(s-j\omega_0)$, and these two voltage sources are actually the control voltage of the RSC and GSC.

However, in a practical wind power generation system, the output voltage of the DFIG system is always kept constant to be the PCC voltage V_{PCC}, while its output current may vary according to output power. Thus, from the perspective of the equivalent circuit seen from the PCC, it is more appropriate to model the small signal equivalent circuit of the DFIG system as a current source I_{SYS} and its parallel impedance Z_{SYS} [29]. On the other hand, the weak network is normally modelled as the voltage source V_{NET} and its series impedance Z_{NET} [29].

Based on the above explanation, the overall small signal equivalent circuit of the investigated DFIG system connected to a weak network is shown in Fig. 5, where Z_{SYS} is the DFIG system impedance in (4), Z_{NET} is the weak network impedance in (5), the V_{NET} is the voltage source of the weak network, and I_{SYS} is the current source presenting the DFIG system.

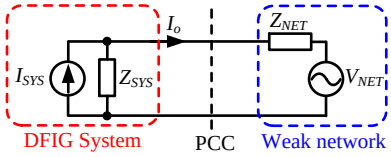

Fig. 5. Small signal equivalent circuit of the DFIG system and the weak network.

Then, according to Fig. 5, the output current I_o of the DFIG system at PCC can be presented as,

$$I_o = \frac{I_{SYS}Z_{SYS}}{Z_{SYS}+Z_{NET}} - \frac{V_{NET}}{Z_{SYS}+Z_{NET}} \tag{6}$$

As illustrated in [29], since the DFIG system is normally able to work stable when the network impedance Z_{NET} is zero (indicating ideal stiff grid), thus the DFIG system, including the variables of I_{SYS} and Z_{SYS}, can be assumed stable. Besides, the network voltage V_{NET} is also normally stable. Based on this description, (6) can be rewritten as,

$$I_o = \left(I_{SYS} - \frac{V_{NET}}{Z_{SYS}}\right)\frac{1}{1+Z_{NET}/Z_{SYS}} \tag{7}$$

Note that the first item of (7) is normally stable as described above and the stability of the overall DFIG system connected to the weak network is determined by the second item of (7), that is, whether the ratio of the network impedance to the DFIG system Z_{NET}/Z_{SYS} satisfies the Nyquist Criterion or not [14], [29].

As discussed in Section IV. B and the experimental results, the amplitude of the undamped HFR is determined by the equivalent resistance of the total impedance including both the DFIG system and the weak network. Note that this equivalent resistance is subject to several influencing factors, including the DFIG machine parameters, LCL filter parameter, RSC and GSC controller parameters, transformer parameters, parallel compensated weak network parameters. Thus, it can be found out that discussing the amplitude of the undamped HFR quantitatively with the consideration of all these above parameters are too complicated and difficult to understand in this paper. Instead, it is assumed that the network inductance L_{NET} remains constant for the weak network, while the shunt capacitance C_{NET} may vary under different conditions due to reactive power compensation and connection / disconnection of sources and loads [26]-[28]. On the other hand, for the DFIG system, the only variables

are the current controller parameters in the RSC and GSC. Therefore, the following stability analysis on the amplitude of undamped HFR using the Nyquist Criterion method will be conducted with different network shunt capacitances and RSC/GSC current controller parameters.

B. Stability analysis using Nyquist Criterion with different network shunt capacitance

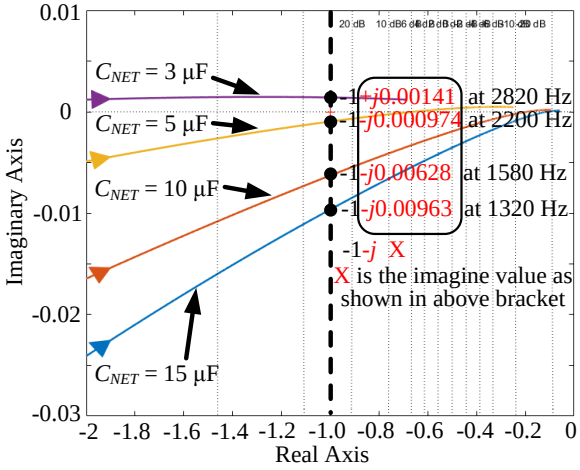

Fig. 6. Nyquist curve of the Z_{NET}/Z_{SYS} under four different network shunt capacitances C_{NET} = 15, 10, 5, 3 μF, K_{prsc} = 2, K_{irsc} = 5, K_{pgsc} = 2 and K_{igsc} = 5.

Fig. 6 shows a part of the Nyquist curve of the Z_{NET}/Z_{SYS} with four different network shunt capacitances C_{NET} = 15, 10, 5, 3 μF, the other parameters are available in Table I. Three conclusions can be drawn from Fig. 6.

1) For all four cases of different network shunt capacitances C_{NET}, their Nyquist curves are very close to the point of (-1,0), indicating that the stability margin is so small that the DFIG system might suffer the HFR at 1320 Hz for C_{NET} = 15 μF; 1580 Hz for C_{NET} = 10 μF; 2200 Hz for C_{NET} = 5 μF; 2820 Hz for C_{NET} = 3 μF. This analysis result matches well with the Bode diagram method results in Fig. 4.

2) For the three cases of C_{NET} = 15, 10 and 5 μF, their Nyquist curves do not encircle the (-1,0), therefore the undamped HFR will exist in steady state. On the contrary, the Nyquist curve with C_{NET} = 3 μF encircles the (-1,0) and the unstable HFR will become divergently instability as a consequence.

This result can also be explained from the perspective of total impedances including both the DFIG system Z_{SYS} and the weak network impedance Z_{NET}. For the cases of C_{NET} = 15, 10 and 5 μF, the Z_{NET}/Z_{SYS} has a negative imaginary part and the total impedance Z_{NET} + Z_{SYS} contains a small positive resistance Z_{SYS} * (-jX), where X is a small positive value of imaginary part as shown in Fig. 6, Z_{SYS} is the pure inductance as shown in Fig. 4. This equivalent small positive resistance causes the undamped HFR in the DFIG system, and at the same time ensures that the undamped HFR exists in steady state.

On the other hand, for the case of C_{NET} = 3 μF, the Z_{NET}/Z_{SYS} has a positive imaginary part, indicating that the Z_{NET} + Z_{SYS} contains a small negative resistance Z_{SYS} * (j0.00141). This equivalent small negative resistance results in the unstable HFR (which eventually results in instability) in the DFIG system.

3) For the three cases of undamped HFR in steady state with C_{NET} = 15, 10 and 5 μF, the value of the equivalent small positive resistance becomes smaller as the C_{NET} becomes smaller, as a consequence the amplitude of the undamped HFR will become larger.

All three conclusions will be validated by the following simulation and experimental results. Based on above explanations, it can be seen that the value of the shunt capacitance C_{NET} in the parallel compensated weak network is 1) very important to the amplitude of the undamped HFR; 2) determining whether the undamped HFR will exist in steady state or enters into unstable HFR and eventually complete instability.

C. Stability analysis using Nyquist Criterion under different current controller parameters

The PI current controller parameters in RSC and GSC are likely to be adjusted in order better to track the rotor current and grid side current, hence it is meaningful to discuss the influence of the PI controller parameters on the amplitude of the undamped HFR. Note that the proportional parameter, but not the integral parameter, is investigated since the proportional parameter has a comparatively larger influence than the integral parameters on the DFIG system impedance in the high frequency range. The PI controller in the RSC is discussed as an example, while the PI controller in the GSC is neglected for the sake of simplicity.

As shown in Fig. 2 and Fig. 3, the PI controllers in the RSC and the GSC are subject to the digital control delay. As a consequence, from the perspective of equivalent impedance, the proportional parameters will behave as the combination of Positive Capacitance (PC) and Positive Resistance (PR) or Negative Resistance (NR) as shown in Fig. 7.

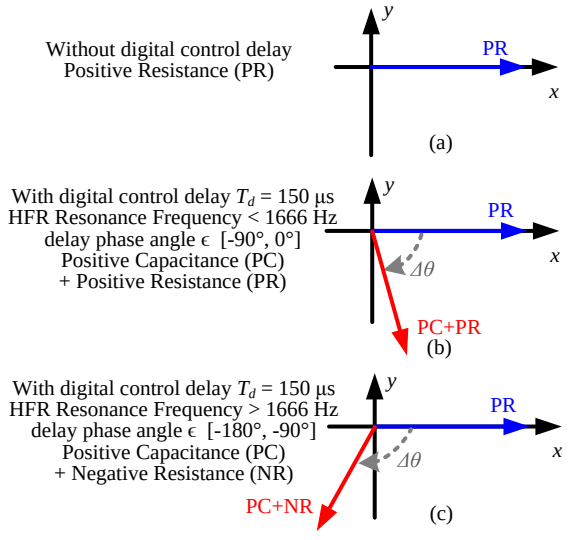

Fig. 7. Equivalent impedance of the proportional parameter K_p under different HFR resonance frequency considering the digital control delay

As it can be seen, the proportional parameter can be regarded as the pure positive resistance when no digital

control delay is considered.

On the other hand, when the digital control delay T_d = 150 μs is included and the HFR resonance frequency is lower than 1666 Hz as shown in Fig. 7(b), the phase delay angle is between -90° and 0°, indicating the PI controller can be equivalently regarded as the combination of the Positive Capacitance (PC) and Positive Resistance (PR).

Moreover, when the digital control delay T_d = 150 μs is included and the HFR resonance frequency is higher than 1666 Hz as shown in Fig. 7(c), the delay phase angle is between -180° and -90°, indicating the PI controller can be equivalently regarded as the combination of the PC and Negative Resistance (NR).

Based on above explanations, Fig. 8 shows that the increase of the proportional parameter will lead to different DFIG system impedance changing. For the HFR frequency lower than 1666 Hz, the increase of the proportional parameter K_p will result in a phase response decrease of the DFIG system below 90° as shown in Fig. 8(a). In contrast, for the HFR frequency higher than 1666 Hz, the increase of the proportional parameter K_p will result in a phase response increase of the DFIG system larger than 90° as shown in Fig. 8(b).

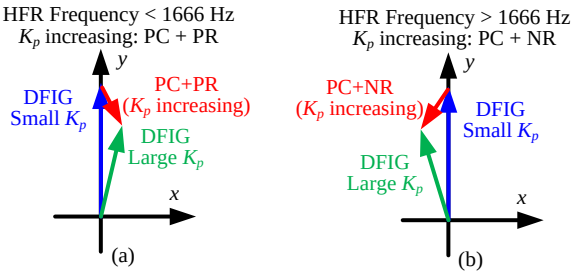

Fig. 8. DFIG system impedance change when the proportional parameter K_p increases, (a) when HFR frequency < 1666 Hz; (b) when HFR frequency > 1666 Hz. PC: Positive Capacitance, PR: Positive Resistance, NR: Negative Resistance .

Then, based on the analysis conducted in Fig. 7 and Fig. 8, when the proportional parameters change, the amplitude of the undamped HFR can be analyzed using the Nyquist Criterion method as shown in Fig. 9.

As shown in Fig. 9(a), for the case of HFR frequency = 1320 Hz when the C_{NET} = 15 μF, the increase of K_{prsc} = 2, 4, 8 helps to move the Nyquist curve away from the (-1,0) and increase the stability margin. Besides, the equivalent positive resistance of the total impedances (including the DFIG system and the weak network) will also increase and the amplitude of the undamped HFR can be suppressed. Thus, it can be verified that the increase of the proportional parameters help to mitigate the amplitude of the undamped HFR when its frequency is below the critical frequency of 1666 Hz.

On the other hand, as shown in Fig. 9(b), for the case of the HFR frequency = 2220 Hz when the C_{NET} = 5 μF, the increase of K_{prsc} from 2 to 4 and 8 causes the DFIG system to change from the undamped HFR in steady state to the unstable HFR since the Nyquist curves encircle the (-1,0). This change can also be explained from the perspective of the equivalent impedance of the entire system. The equivalent total impedance is small positive resistance for the case of K_{prsc} = 2; however, for the case of K_{prsc} = 4 and 8, the equivalent total impedance is small negative resistance, and as a consequence the unstable HFR will appear and eventually results in instability.

Based on the above discussions, it can be found that the proportional parameters are important to the behavior of HFR by either changing the amplitude of the undamped HFR or causing a complete unstable HFR.

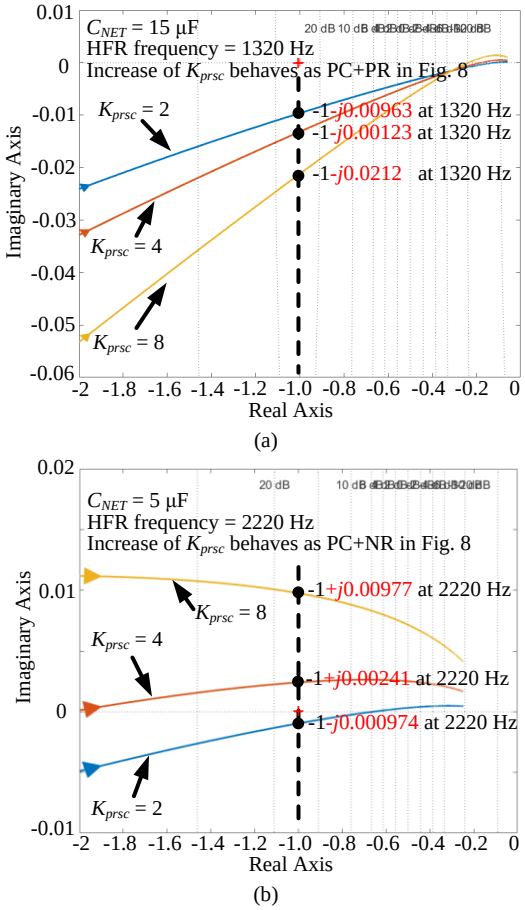

Fig. 9. Nyquist curve of different Z_{NET}/Z_{SYS}, K_{prsc} = 2, 4, 8, K_{irsc} = 5, K_{pgsc} = 2 and K_{igsc} = 5. (a) when C_{NET} = 15 μF, HFR frequency = 1320 Hz; (b) when C_{NET} = 5 μF, HFR frequency = 2220 Hz.

D. Boundary of the undamped HFR and unstable HFR

As discussed in Section IV. B and C, the HFR stability analysis with different network shunt capacitance and different current controller parameters are investigated in Fig. 6 and Fig. 9 respectively. The Nyquist Curves in Fig. 6 and Fig. 9 show that whether the intersection point (black dots in Fig. 6 and Fig. 9) between the Nyquist Curve Z_{NET}/Z_{SYS} and the unit circle is located below (or above) the imaginary axis determines the occurrence of the undamped HFR (or unstable HFR).

1) To explain in more details, when the intersection point (black dots in Fig. 6 and Fig. 9) between the Nyquist Curve Z_{NET}/Z_{SYS} and the unit circle is below imaginary axis, indicating a negative imaginary part,

$$Z_{NET}/Z_{SYS} = -1 - jX \tag{8a}$$

where, X is a very small positive value according to the Nyquist Curve.

Then, the total impedance of the DFIG system and the

weak network can be presented as,

$$Z_{NET} + Z_{SYS} = -jX * Z_{SYS} = -jX * jS = X * S \quad (8b)$$

where, the Z_{SYS} can be regarded as jS (S is also a very small positive value) since the DFIG system behaves as positive inductive with phase response = 90 degree in the HFR frequency range as shown in Fig. 4.

Thus, it can be seen that the total impedance has positive resistance in this case, and the undamped HFR will occur in steady state.

2) In contrary, when the intersection point (black dots in Fig. 6 and Fig. 9) between the Nyquist Curve Z_{NET}/Z_{SYS} and the unit circle is above imaginary axis, indicating a positive imaginary part,

$$Z_{NET}/Z_{SYS} = -1 + jX \quad (9a)$$

Then, the total impedance of the DFIG system and the weak network can be presented as,

$$Z_{NET} + Z_{SYS} = jX * Z_{SYS} = jX * jS = -X * S \quad (9b)$$

Thus, it can be seen that the total impedance has negative resistance in this case, and the unstable HFR will occur to divergence.

3) Therefore, it can be concluded that whether the intersection point (black dots in Fig. 6 and Fig. 9) between the Nyquist Curve Z_{NET}/Z_{SYS} and the unit circle located below or above the imaginary axis is the boundary of the undamped HFR and unstable HFR, i.e., the undamped HFR happens if the intersection point is below the imaginary axis which indicates a positive resistance of the total impedance; or the unstable HFR happens if the intersection point is above the imaginary axis which indicates a negative resistance of the total impedance.

V. Simulation and Experimental Validation

In order to validate the analysis on the undamped HFR and unstable HFR using the proposed Nyquist Criterion based method, the experimental and simulation validation on a small scale DFIG system is provided. For the steady state undamped HFR performance, the experimental results are given, and the undamped HFR with different frequency and amplitude can be observed. However, the unstable HFR may trigger the over current and over voltage protection, and may even cause damage to the DFIG system experimental hardware. Therefore, instead, the simulation results of the unstable HFR which results in instability are provided in MATLAB Simulink.

A. Control diagram

Fig. 10 shows the control diagram of the DFIG system and its parameters can be found in Table I. An enhanced Phase Locked Loop (PLL) is employed to provide the grid voltage fundamental synchronous angular speed ω_1 and angle θ_1, while an encoder gives out the DFIG rotor position θ_r and speed ω_r.

The rotor current $\boldsymbol{I}^{+}_{rdq}$ is first sampled and then controlled based on the reference value $\boldsymbol{I}^{+*}_{rdq}$ with a PI controller to output the harvested wind energy. The output of the rotor current PI closed-loop control $\boldsymbol{V}^{+}_{rdqPI}$ and a decoupling compensation are added, giving out the rotor control voltage $\boldsymbol{V}^{+}_{rdq}$, which is then transformed to the rotor stationary frame and delivered as the input to the Space Vector Pulse Width Modulation (SVPWM).

As for the GSC control, the dc-link voltage V_{dc} is regulated by a PI controller, and its output is delivered as the converter side inductance filter current reference $\boldsymbol{I}^{+*}_{fdq}$, which is used to regulate the converter side inductance filter current $\boldsymbol{I}^{+}_{fdq}$ by a PI controller. Similarly, the GSC control voltage $\boldsymbol{V}^{+}_{gdq}$ can be obtained by a PI current controller output and the decoupling compensation unit.

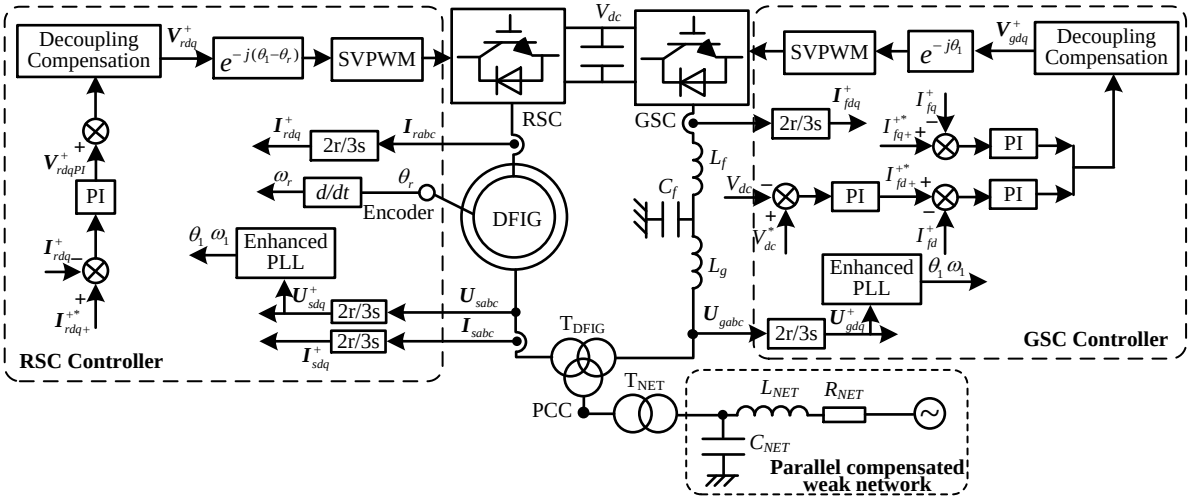

Fig. 10. Control diagram of the DFIG system including the parallel compensated weak network. RSC: Rotor Side Converter, GSC: Grid Side Converter.

B. Experimental setup

A 7.5 kW test rig is built up for the purpose of experimental validation and shown in Fig. 11, and the DFIG system parameters can be found in Table I.

The main differences between the commercial DFIG system discussed in Fig. 10 and the experimental DFIG system in Fig. 11 are, 1) the three-terminal transformer and the two-terminal transformer in the commercial DFIG do not exist in the experimental DFIG; 2) in order to prevent the grid connection inrush and the inner system current circulation, a transformer is connected between the DFIG stator winding and thr PCC in the experimental DFIG system in Fig. 11, but it does not change the voltage level

between the primary and secondary sides.

The DFIG is externally driven by a prime motor, and two 5.5-kW Danfoss motor drives are used for the GSC and the RSC, both of which are controlled with dSPACE 1006 control system. The rotor speed is set to 1200 rpm (0.8 pu), with the synchronous speed of 1500 rpm (1.0 pu). The dc-link voltage is 650 V. The DFIG stator output active and reactive power is 5 kW and 0 Var. The AD sampling frequency and switching frequency of both converters are 10 kHz and 5 kHz respectively.

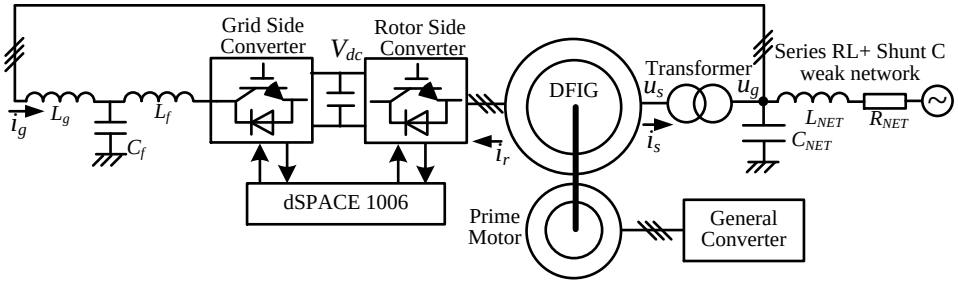

Fig. 11. Setup of a 7.5 kW experimental DFIG system test rig

C. Experimental result of the undamped HFR in steady state

Fig. 12 shows the experimental result of no HFR in the DFIG system when no shunt capacitor in the weak grid network, R_{NET} = 3 mΩ, L_{NET} = 1.5 mH, rotor speed = 1200 rpm (sub- synchronous speed). No HFR will occur in this case due to the inductive character of both the DFIG system and the weak network at the high frequency range.

Fig. 13 to Fig. 15 show the experimental results of the undamped HFR in the DFIG system when the shunt capacitor C_{NET} = 15, 10, 5 μF, R_{NET} = 3 mΩ, L_{NET} = 1.5 mH, rotor speed = 1200 rpm (sub- synchronous speed). By comparing the experimental results at different network shunt capacitances C_{NET}, it can be seen that the amplitude of the undamped HFR becomes increasingly larger when the C_{NET} becomes smaller as shown in Table II. This result matches well with the theoretical analysis in Fig. 6.

On the other hand, Fig. 16 to Fig. 18 show the experimental results of the undamped HFR in the DFIG system when the shunt capacitor C_{NET} = 15, 10, 5 μF, R_{NET} = 3 mΩ, L_{NET} = 1.5 mH, rotor speed = 1700 rpm (super-synchronous speed). Similar results as the case at sub-synchronous speed can be obtained as shown in Table II, i.e., smaller network shunt capacitance C_{NET} leads to larger amplitude of the undamped HFR,. Thus, these results at super- synchronous speed also help to validate the analysis in Fig. 6.

TABLE II. THEORETICAL AND EXPERIMENTAL RESULTS OF HFR IN STATOR VOLTAGE

C_{NET}	Theoretical Analysis	Experimental Results	
		Sub- synchronous speed 1200 rpm	Super- synchronous speed 1700 rpm
15 μF	1316 Hz	1475 Hz: 5.2%	1470 Hz: 5.8%
10 μF	1575 Hz	1600 Hz: 32%	1600 Hz: 35%
5 μF	2195 Hz	2250 Hz: 47%	2125 Hz: 42%

Furthermore, by comparing the experimental results with same network shunt capacitance C_{NET}, but at different rotor speeds, i.e., Fig. 13 and Fig. 16 with the same C_{NET} = 15 μF but with different rotor speed = 1200 rpm and 1700 rpm; Fig. 14 and Fig. 17 with the same C_{NET} = 10 μF but with different rotor speed = 1200 rpm and 1700 rpm; Fig. 15 and Fig. 18 with the same C_{NET} = 5 μF but with different rotor speed = 1200 rpm and 1700 rpm. It can be found that the amplitude of the undamped HFR is almost constant regardless of the different rotor speeds as shown in Table II. These experimental results help to validate that the rotor speed is not important to the amplitude of the undamped HFR.

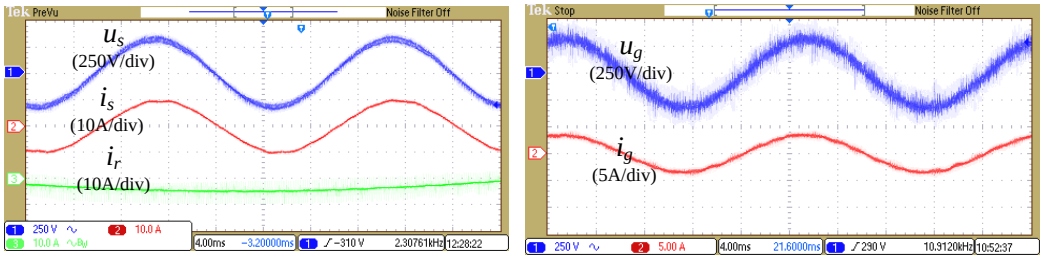

Fig. 12. Experimental result of no HFR in the DFIG system when no shunt capacitor in the weak grid network, R_{NET} = 3 mΩ, L_{NET} = 1.5 mH, rotor speed = 1200 rpm (sub- synchronous speed)

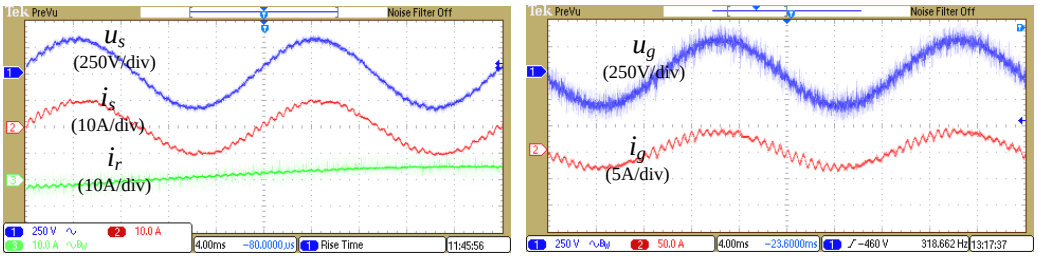

Fig. 13. Experimental result of the undamped HFR in the DFIG system when shunt capacitance C_{NET} = 15 μF in the weak grid network, R_{NET} = 3 mΩ, L_{NET} = 1.5 mH, rotor speed = 1200 rpm (sub- synchronous speed)

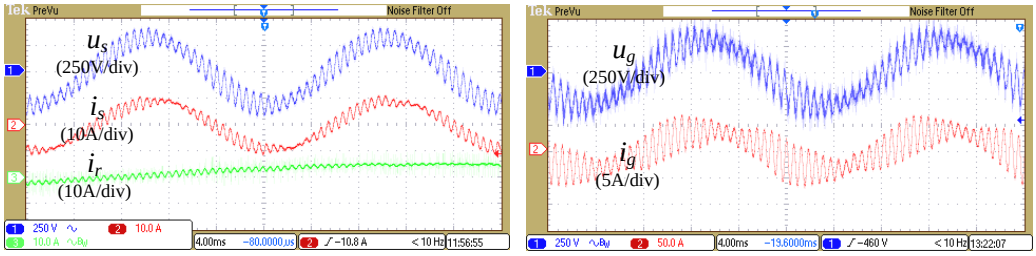

Fig. 14. Experimental result of the undamped HFR in the DFIG system when shunt capacitance C_{NET} = 10 μF in the weak grid network, R_{NET} = 3 mΩ, L_{NET} = 1.5 mH, rotor speed = 1200 rpm (sub- synchronous speed)

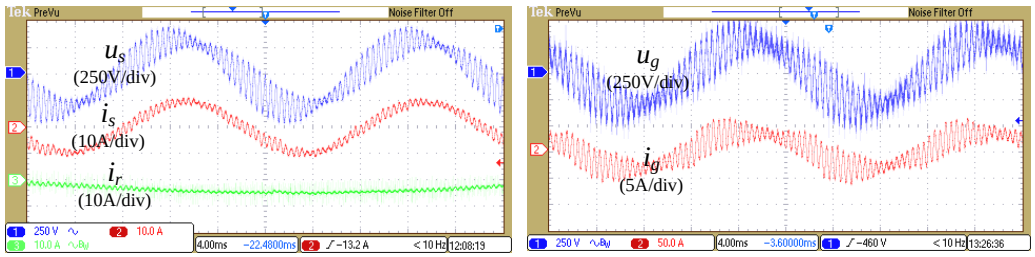

Fig. 15. Experimental result of the undamped HFR in the DFIG system when shunt capacitance C_{NET} = 5 μF in the weak grid network, R_{NET} = 3 mΩ, L_{NET} = 1.5 mH, rotor speed = 1200 rpm (sub- synchronous speed)

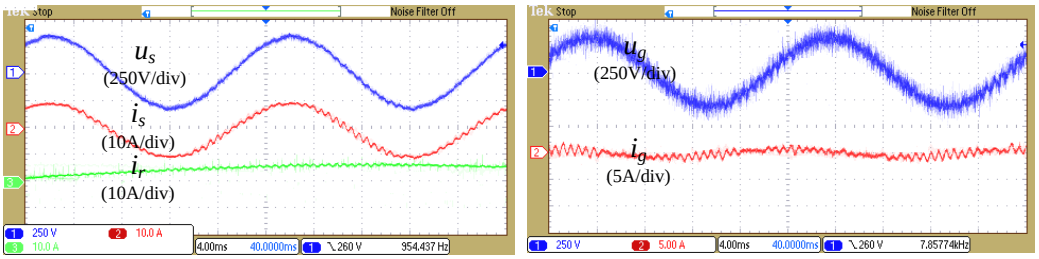

Fig. 16. Experimental result of the undamped HFR in the DFIG system when shunt capacitance C_{NET} = 15 μF in the weak grid network, R_{NET} = 3 mΩ, L_{NET} = 1.5 mH, rotor speed = 1700 rpm (super- synchronous speed)

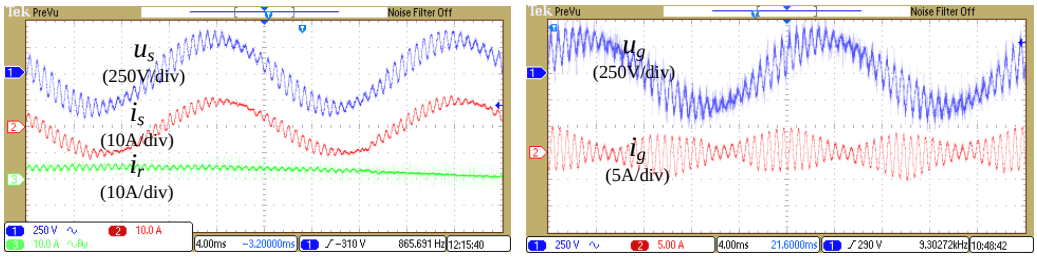

Fig. 17. Experimental result of the undamped HFR in the DFIG system when shunt capacitance C_{NET} = 10 μF in the weak grid network, R_{NET} = 3 mΩ, L_{NET} = 1.5 mH, rotor speed = 1700 rpm (super- synchronous speed)

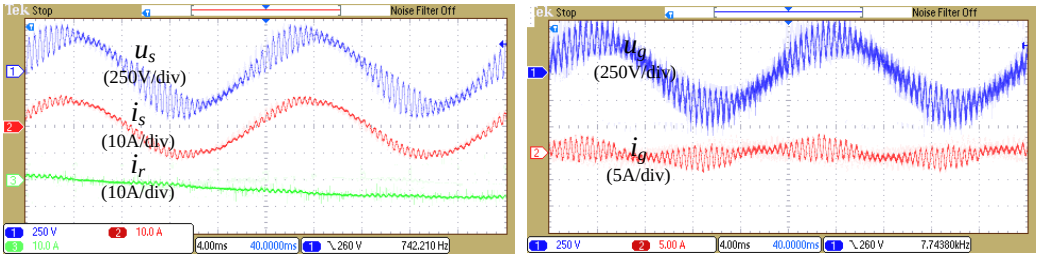

Fig. 18. Experimental result of the undamped HFR in the DFIG system when shunt capacitance C_{NET} = 5 μF in the weak grid network, R_{NET} = 3 mΩ, L_{NET} = 1.5 mH, rotor speed = 1700 rpm (super- synchronous speed)

D. Simulation result of the unstable HFR

Simulations are done for the validation of the unstable HFR (which results in instability). The parameters of the simulated DFIG system are the same as the experimental one.

Before showing the simulation results of the unstable HFR, the results of the undamped HFR need to be shown in order to prove that the simulation model is identical with the experiment setup. Note that in order to save space in this paper, only the simulation results of the stator voltage and its FFT analysis will be provided with the network shunt capacitance C_{NET} = 15, 10, 5 μF at sub- synchronous speed as shown in Fig. 19.

As it can be seen, the simulation results of stator voltage with different network shunt capacitance C_{NET} = 15, 10, 5 μF contain the undamped HFR with different frequency and amplitude, i.e., the undamped HFR = 1410 Hz of 5.5% for the case of C_{NET} = 15 μF; the undamped HFR = 1610 Hz of 31.5% for the case of C_{NET} = 10 μF; the undamped HFR = 2215 Hz of 38.1% for the case of C_{NET} = 5 μF. By comparing the simulation results in Fig. 19 and the experimental results in Fig. 13 to Fig. 15 and Table II, it can be found out that the simulation results match well with the experimental results, thus it can be concluded that the simulation model of the DFIG system is identical to the experimental setup, thereby the simulation model can be adopted to validate the unstable HFR performance in the DFIG system when the small network shunt capacitance C_{NET} = 3 μF is applied. This unstable HFR simulation results are shown in Fig. 20.

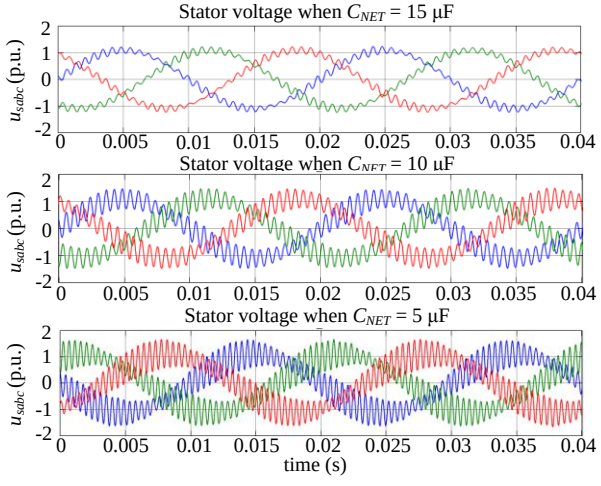

(a)

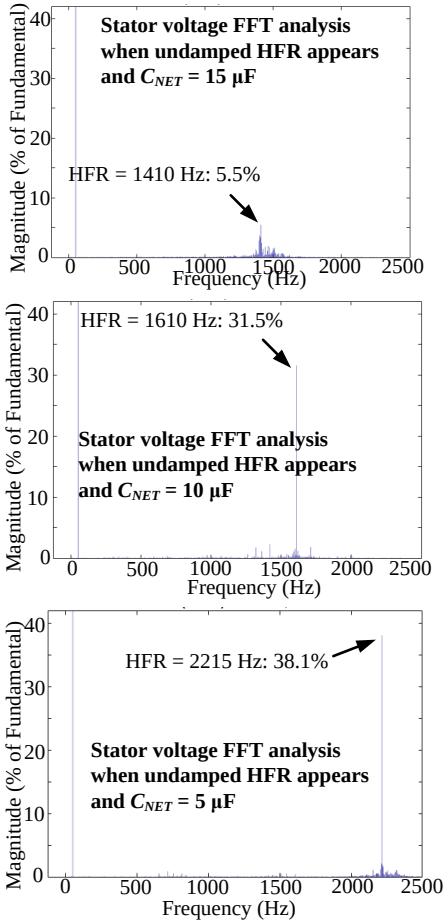

(b)

Fig. 19. Simulation results of undamped HFR when shunt capacitance C_{NET} = 15, 10, 5 μF, R_{NET} = 3 mΩ, L_{NET} = 1.5 mH in the weak grid network, rotor speed = 1200 rpm (sub- synchronous speed) (a) stator voltage; (b) FFT analysis of the stator voltage.

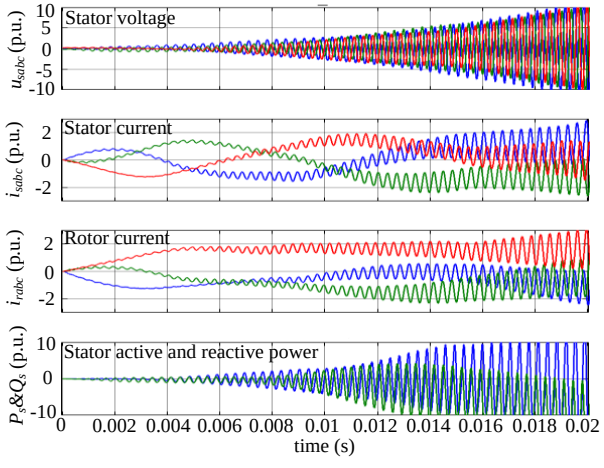

(a)

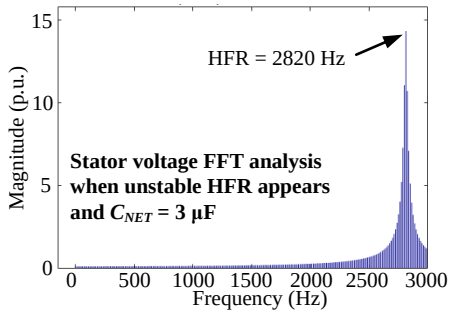

(b)

Fig. 20. Simulation results of the unstable HFR when shunt capacitance C_{NET} = 3 μF, R_{NET} = 3 mΩ, L_{NET} = 1.5 mH in the weak grid network, rotor speed = 1200 rpm (sub- synchronous speed) (a) system performance; (b) FFT analysis of the stator voltage.

Fig. 20 shows the simulation results of the unstable HFR in the DFIG system when shunt capacitance C_{NET} = 3 μF, R_{NET} = 3 mΩ, L_{NET} = 1.5 mH in the weak grid network, rotor speed = 1200 rpm (sub- synchronous speed).

As it can be observed from Fig. 20(a), the DFIG system suffers the unstable HFR frequency = 2820 Hz and complete instability will eventually be the consequence. The FFT analysis of the stator voltage shown in Fig. 20(b) matches well with the theoretical analysis in Fig. 6. Note that the unstable HFR does not stay in steady state, but causes instability eventually, and the stator voltage, rotor current, stator current and output active power and reactive power all contain large amplitudes, which will trigger the over current and over voltage protection in practice. Thus, the unstable HFR can be validated by the simulation results when the network shunt capacitance is too small as C_{NET} = 3 μF.

VI. Conclusion

This paper has investigated the amplitude of the undamped HFR (which exists in steady state) as well as the unstable HFR (which eventually results in instability) in the DFIG system under the parallel compensated weak network using the Nyquist Criterion method. Several conclusions can be obtained,

1) Compared with the conventional Bode diagram based analysis method, the proposed Nyquist Criterion analysis method can identify the HFR frequency and estimate the amplitude of the undamped HFR at the same time; moreover, it can also identify the occurrence of the unstable HFR.

2) The smaller network shunt capacitance C_{NET} in the parallel compensated weak network results in a larger amplitude and higher frequency of the undamped HFR. In extreme cases, a smaller C_{NET} may even cause the unstable HFR by encircling the (-1,0) with the Nyquist curve of Z_{NET}/Z_{SYS}.

3) The proportional parameters in the PI current controller in the RSC and GSC are relatively important to the amplitude of the undamped HFR, but not sensitive to the HFR frequency;

4) The rotor speed is not sensitive to the amplitude and frequency of the undamped HFR.

REFERENCES

[1] F. Blaabjerg, and K. Ma, "Future on Power Electronics for Wind Turbine Systems," *IEEE J. Emer. Sel. Topics Power Electron*., vol. 1, no. 3, pp. 139-152, Sep. 2013.

[2] K. Ma, L. Tutelea, I. Boldea, D. M. Ionel, F. Blaabjerg, "Power Electronic Drives, Controls, and Electric Generators for Large Wind Turbines–An Overview", *Electric Power Components and Systems*, vol. 43, no. 12, pp. 1406-1421, 2015.

[3] V. Yaramasu, B. Wu, P. C. Sen, S. Kouro, and M. Narimani, "High-power wind energy conversion systems: State-of-the-art and emerging technologies," *Proceedings of the IEEE*, vol. 103, no. 5, pp. 740 – 788, 2015.

[4] H. Nian, P. Cheng, and Z. Q. Zhu, "Coordinated Direct Power Control of DFIG System Without Phase-Locked Loop Under Unbalanced Grid Voltage Conditions," *IEEE Trans. Power Electron*., vol. 31, no. 4, pp. 2905 - 2918, Apr. 2016.

[5] H. Nian, P. Cheng, and Z. Q. Zhu, "Independent Operation of DFIG-Based WECS Using Resonant Feedback Compensators Under Unbalanced Grid Voltage Conditions," *IEEE Trans. Power Electron*., vol. 30, no. 7, pp. 3650 - 3661, July 2015.

[6] P. Cheng, H. Nian, C. Wu and Z. Q. Zhu, "Direct Stator Current Vector Control Strategy of DFIG Without Phase-Locked Loop During Network Unbalance," *IEEE Trans. Power Electron*., vol. 32, no. 1, pp. 284 - 297, Jan. 2017.

[7] J. Hu, B. Wang, W. Wang, H. Tang, Y. Chi, Q. Hu. "Small Signal Dynamics of DFIG-based Wind Turbines during Riding Through Symmetrical Faults in Weak AC Grid," *IEEE Trans. Energy Convers*., accepted & in press.

[8] J. Hu, L. Sun, X. Yuan, S. Wang, Y. Chi. "Modeling of Type 3 Wind Turbine with df/dt Inertia Control for System Frequency Response Study," *IEEE Trans. Power Systems*, accepted & in press.

[9] I. Vieto, and J. Sun, "Damping of Subsynchronous Resonance Involving Type-III Wind Turbines," *in Proc. Control and Modeling for Power Electronics* (COMPEL), pp. 1-8, 2015.

[10] I. Vieto, and J. Sun, "Small-Signal Impedance Modeling of Type-III Wind Turbine," *in Proc. Power & Energy Society General Meeting* (PESG), pp. 1-5, 2015.

[11] I. Vieto, and J. Sun, "Real-time Simulation of Subsynchronous Resonance in Type-III Wind Turbines," *in Proc. Control and Modeling for Power Electronics* (COMPEL), pp. 1-8, 2014

[12] Z. Miao, "Impedance-Model-Based SSR Analysis for Type 3 Wind Generator and Series-Compensated Network," *IEEE Trans. Energy Convers.*, vol. 27, no. 4, pp. 984–991, Dec. 2012.

[13] L. Piyasinghe, Z. Miao, J. Khazaei, and L. Fan, "Impedance Model-Based SSR Analysis for TCSC Compensated Type-3 Wind Energy Delivery Systems," *IEEE Trans. Sustainable Energy.*, vol. 6, no. 1, pp. 179–187, Jan. 2015.

[14] L. Fan, and Z. Miao, "Nyquist-Stability-Criterion-Based SSR Explanation for Type-3 Wind Generators," *IEEE Trans. Energy Convers.*, vol. 27, no. 3, pp. 807–809, Sep. 2012.

[15] L. Wang, X. Xie, Q. Jiang, H. Liu, Y. Li, and H. Liu, "Investigation of SSR in Practical DFIG-Based Wind Farms Connected to a Series-Compensated Power System," *IEEE Trans. on Power Syst.*, vol. 30, no. 5, pp. 2772 – 2779, Sep. 2015.

[16] L. Fan, R. Kavasseri, Z. Miao, and C. Zhu, "Modeling of DFIG-Based Wind Farms for SSR Analysis," *IEEE Trans. on Power Delivery.* vol. 25, no. 4, pp. 2073-2082, Oct. 2010.

[17] H. Liu, X. Xie, C. Zhang, Y. Li, H. Liu, and Y. Hu, "Quantitative SSR Analysis of Series- Compensated DFIG-Based Wind Farms using Aggregated RLC Circuit Model," *IEEE Trans. on Power Syst.*, early access.

[18] L. Fan, C. Zhu, Z. Miao, and M. Hu, "Modal Analysis of a DFIG-Based Wind Farm Interfaced With a Series Compensated Network," *IEEE Trans. Energy Convers.*, vol. 26, no. 4, pp. 1010–1020, Dec. 2011.

[19] H. A. Mohammadpour, and E. Santi, "Sub-synchronous resonance analysis in DFIG-based wind farms: Definitions and problem

identification — Part I," in *Proc. of IEEE Energy Conversion Congress and Exposition (ECCE)*, pp. 812 – 819, Sept. 2014.
[20] L. Fan, and Z. Miao, "Mitigating SSR Using DFIG-Based Wind Generation," *IEEE Trans. Sustain. Energy*, vol. 3, no. 3, pp. 349–358, July 2012.
[21] H. A. Mohammadpour, and E. Santi, "SSR Damping Controller Design and Optimal Placement in Rotor-Side and Grid-Side Converters of Series-Compensated DFIG-Based Wind Farm," *IEEE Trans. on Sustain. Energy*, vol. 6, no. 2, pp. 388 - 399, April, 2015.
[22] A. E. Leon, and J. A. Solsona, "Sub-Synchronous Interaction Damping Control for DFIG Wind Turbines," *IEEE Trans. on Power Syst.* vol. 30, no. 1, pp. 419-428, Jan. 2015.
[23] P. Huang, M. Moursi, W. Xiao, and J. Kirtley, "Subsynchronous Resonance Mitigation for Series-Compensated DFIG-Based Wind Farm by Using Two-Degree-of-Freedom Control Strategy," *IEEE Trans. Power Syst*., vol. 30, no. 3, pp. 1442-1454, May 2015.
[24] A. Leon, "Integration of DFIG-Based Wind Farms Into Series-Compensated Transmission Systems," *IEEE Trans. on Sustain. Energy*, vol. 7, no. 2, pp. 451 - 460, April 2016.
[25] H. A. Mohammadpour, and E. Santi, "Sub-synchronous resonance analysis in DFIG-based wind farms: Mitigation methods — TCSC, GCSC, and DFIG controllers — Part II," in *Proc. of IEEE Energy Conversion Congress and Exposition (ECCE)*, pp. 1550 – 1557, Sept. 2014.
[26] Y. Song, X. Wang, F. Blaabjerg, "Impedance-Based Super-Synchronous Resonance Analysis of DFIG System in Weak Grids," IEEE Trans. Power Electron., vol. PP, no. 99, early access, 2016.
[27] Y. Song, X. Wang, and F. Blaabjerg, "High Frequency Resonance Damping of DFIG based Wind Power System under Weak Network," *IEEE Trans. Power Electron*., vol. PP, no. 99, early access.
[28] Y. Song, F. Blaabjerg, "Wide Frequency Band Active Damping Strategy for DFIG System High Frequency Resonance," IEEE Trans. Energy., Convers., vol. PP, no. 99, early access, 2016.
[29] J. Sun, "Impedance-based stability criterion for grid-connected inverters," *IEEE Trans. Power Electron*., vol. 26, no. 11, pp. 3075–3078, Nov. 2011.

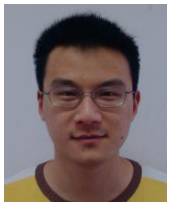

Yipeng Song was born in Hangzhou, China. He received the B.Sc. degree and Ph.D. degree both from the College of Electrical Engineering, Zhejiang University, Hangzhou, China, in 2010 and 2015. He is currently working as a Postdoc at the Department of Energy Technology in Aalborg University, Denmark. His current research interests are motor control with power electronics devices in renewable-energy conversion, particularly the control and operation of doubly fed induction generators for wind power generation.

Frede Blaabjerg (S'86–M'88–SM'97–F'03) was with ABB-Scandia, Randers, Denmark, from 1987 to 1988. From 1988 to 1992, he was a Ph.D. Student with Aalborg University, Aalborg, Denmark. He became an Assistant Professor in 1992, Associate Professor in 1996, and Full Professor of power electronics and drives in 1998. His current research interests include power electronics and its applications such as in wind turbines, PV systems, reliability, harmonics and adjustable speed drives.

He has received 17 IEEE Prize Paper Awards, the IEEE PELS Distinguished Service Award in 2009, the EPE-PEMC Council Award in 2010, the IEEE William E. Newell Power Electronics Award 2014 and the Villum Kann Rasmussen Research Award 2014. He was an Editor-in-Chief of the IEEE TRANSACTIONS ON POWER ELECTRONICS from 2006 to 2012. He is nominated in 2014 and 2015 by Thomson Reuters to be between the most 250 cited researchers in Engineering in the world.